EES Catalysis

PAPER

View Article Online
View Journal | View Issue

Cite this: *EES Catal.*, 2025, 3, 1358

Dynamic evolution of self-renewal Fe–N–C catalysts for the acidic oxygen reduction reaction†

Fangzhou Liu,[a] Leo Lai,[a] Zhongyuan Guo,[bc] Fangxin She,[a] Justin Prabowo,[a] Hao Li,*[b] Li Wei*[a] and Yuan Chen*[a]

Heterogeneous molecular Fe–N–C catalysts hold promise for the oxygen reduction reaction (ORR), but their stability in acidic media remains a bottleneck. Here, we report the synthesis of a self-renewal Fe–N–C catalyst by uniformly polymerizing an iron polyphthalocyanine (FePPc) shell around carbon nanotubes (CNTs) *via* a microwave-assisted method. This FePPc/CNT catalyst achieves a much higher Fe mass loading (2.92 wt%) compared to directly depositing iron phthalocyanine (FePc) molecules on CNTs (FePc/CNT, 0.80 wt%) while maintaining a similar density of exposed Fe–N_4 sites to electrolytes. FePPc/CNT exhibits superior ORR activity in 0.1 M $HClO_4$ electrolyte with a half-wave potential ($E_{1/2}$) of 0.74 V (*vs.* reversible hydrogen electrode), a low Tafel slope of 51 mV dec^{-1}, and a high turnover frequency (TOF) of 0.98 $site^{-1}$ s^{-1}. Density functional theory (DFT) calculations attribute this enhanced activity to strong FePPc–CNT interactions that facilitate efficient electron transfer and favorable reaction energetics. Critically, FePPc/CNT demonstrates enhanced stability in the acidic electrolyte, retaining ~80% of its initial current density after 24 h of the chronoamperometric test, outperforming FePc/CNT (42% after 5 h) and physically mixed FePPc and CNTs (49% after 24 h). Quantitative analysis reveals a unique self-renewal mechanism involving layer-by-layer shedding of FePPc, which exposes fresh active sites to sustain catalytic activity. At the same time, detached FePPc fragments sediment on CNTs. Furthermore, leached Fe ions migrate onto CNTs and aggregate into FeO_x nanoclusters, eventually leading to irreversible deactivation. These findings provide new insights for designing durable Fe–N–C catalysts for various reactions.

Received 28th March 2025,
Accepted 21st July 2025

DOI: 10.1039/d5ey00092k

rsc.li/eescatalysis

Broader context

Developing efficient and durable catalysts for the oxygen reduction reaction (ORR) is crucial for advancing sustainable energy technologies, particularly in fuel cells and metal–air batteries. Despite significant progress, the reliance on expensive platinum-based catalysts remains a key challenge in commercializing these technologies. This study presents a novel non-precious metal single-atom catalyst with enhanced ORR activity and durability, offering a cost-effective alternative to Pt-based materials. Our findings demonstrate that incorporating catalytic active single-atom sites into polymeric structures is beneficial in increasing their stability. The close interaction between carbon nanotube substrates and polymeric shells can improve catalyst activity. Critically, the polymeric shell has a unique self-renewal capability that can regenerate its catalytic surface *via* layer-by-layer shedding, leading to significantly improved stability in acidic electrolytes. By addressing fundamental limitations in non-precious metal single-atom catalysts, this work contributes to developing scalable, high-performance electrocatalysts to accelerate the transition toward clean energy solutions.

Introduction

The oxygen reduction reaction (ORR) is critical in various electrochemical energy conversion and storage devices, such as proton exchange membrane fuel cells and metal–air batteries.[1–3] The dominant ORR catalysts are based on expensive platinum (Pt) or Pt alloys.[4–6] Significant research efforts have been devoted to transition metal (M) and nitrogen (N) co-doped carbon (M–N–C) catalysts.[7–12] In particular, some state-of-the-art Fe–N–C catalysts

[a] *School of Chemical and Biomolecular Engineering, The University of Sydney, Darlington, New South Wales, 2006, Australia. E-mail: l.wei@sydney.edu.au, yuan.chen@sydney.edu.au*
[b] *Advanced Institute for Materials Research (WPI-AIMR), Tohoku University, Sendai, 980-8577, Japan. E-mail: li.hao.b8@tohoku.ac.jp*
[c] *College of Environmental and Resource Sciences, Zhejiang University, Hangzhou, 310058, China*

† Electronic supplementary information (ESI) available. See DOI: https://doi.org/10.1039/d5ey00092k

have exhibited catalytic activity comparable to Pt-based catalysts.[13–15] For example, their half-wave potential ($E_{1/2}$) approached 0.85 V_{RHE} (*vs.* reversible hydrogen electrode (RHE)) with 10 000 stable cyclic voltammetry (CV) cycles in 0.5 M H_2SO_4 acidic electrolytes.[16] Fe–N–C catalysts are usually synthesized by high-temperature (600–1100 °C) pyrolysis of Fe-containing compounds and carbon precursors.[17,18] During pyrolysis, chemical bonds in original precursors are broken, and Fe–N_4 catalytically active sites are formed and incorporated into carbon substrates.[19] However, due to the high synthesis temperatures, precisely controlling the atomic structures of Fe–N–C catalysts is difficult.

Alternatively, M–N–C catalysts can be produced by anchoring small organic molecules containing Fe–N–C atomic structures on carbon substrates as heterogeneous molecular catalysts. For example, iron phthalocyanine (FePc) molecules have been anchored on carbon materials, demonstrating promising catalytic activities for the ORR in alkaline electrolytes.[20–25] However, in general, such heterogeneous molecular M–N–C catalysts exhibit poor stability in acidic electrolytes, which has been attributed to the detachment of small organic molecules from carbon substrates and rapid demetallation of their Fe–N–C sites (Table S1 in the ESI†).[26–29] Several recent studies have explored incorporating FePc molecules into polymeric structures, *e.g.*, polyphthalocyanine (FePPc) constructed from repeating phthalocyanine units linked *via* covalent bonds, to improve their catalytic activity and stability.[30,31] For instance, Yang *et al.* reported a low-temperature pyrolysis method (<400 °C) to modify functional groups of an FePPc layer anchored on acetylene black. Specifically, FePPc with –COOH functional groups demonstrated an $E_{1/2}$ of 0.8 V_{RHE} and retained 73% of its initial current density after 5 h of chronoamperometric stability tests.[30] However, the stability test time of 5 h is too short, and the catalyst degradation mechanism is not elucidated. More stable polymer-based heterogeneous molecular M–N–C catalysts are critical for their practical applicability.

In this work, we synthesize a heterogeneous molecular M–N–C catalyst by *in situ* formation of a thin layer of an FePPc polymeric shell around a carbon nanotube (CNT) core. The low-temperature microwave-assisted polymerization preserves the original molecular structures of FePPc, resulting in well-defined catalytically active sites (FePc) in the FePPc shell. The CNT core provides a fast electron transfer path. The close interactions between the *in situ* polymerized FePPc shell and CNT core lead to increased catalytic activity for the ORR compared to individual FePc molecules adsorbed on CNTs or physically mixed FePPc and CNTs. Importantly, this catalyst, with a well-defined structure, enables us to systematically analyze its degradation pathways using various characterization tools. We discover a catalyst surface self-renewal mechanism. The surface of the FePPc shell continuously sheds off as FePPc fragments in electrolytes during the ORR in acidic electrolytes. The new FePPc surfaces underneath are exposed to electrolytes, providing new catalytically active sites that help maintain the initial catalytic activity for the ORR for much longer. Furthermore, the shed FePPc fragments sediment on other locations of CNTs. Leached Fe ions and Fe in sedimented FePPc fragments aggregate into FeO_x nanoclusters with lower catalytic activity. These findings provide new insights into designing heterogeneous molecular M–N–C catalysts with improved activity and stability.

Experimental

Chemicals

Commercial FePc (95%, PorphyChem Inc.) was first purified by triple sublimation before usage. 1,2,4,5-Tetracyanobenzene (TCNB, 97%), 1,8-diazabicyclo[5.4.0]undec-7-ene (DBU, 98%), nitric acid (HNO_3, 70%), perchloric acid ($HClO_4$, 70%), hydrochloric acid (HCl, 37%), iron chloride ($FeCl_2$, anhydrous, 99.9%), sodium acetate (CH_3COONa, >99%), hydroxylamine hydrochloride ($NH_2OH{\cdot}HCl$, >99%), ammonium iron sulfate dodecahydrate ($NH_4Fe(SO_4)_2{\cdot}12H_2O$, >99%), sodium nitrite ($NaNO_2$, >99.9%), 1-pentanol (>99%), acetic acid (CH_3COOH, >99%), 1,10-phenanthroline (*o*-phen, anhydrous, >99%), ethanol (200 proof, anhydrous, >99.5%), isopropyl alcohol (IPA, 99%), and *N*,*N*-dimethylformamide (DMF, anhydrous, 99.8%) were purchased from Sigma-Aldrich and used without any treatment. O_2 (4.5 grade), Ar (5.0 grade), and 5% H_2/Ar were purchased from BOC Australia. Multi-walled CNTs with a diameter of 10–20 nm were purchased from CNano Inc. CNTs were purified before being used for catalyst synthesis. Deionized water (DI H_2O) was produced from a Merck MilliQ water system.

CNT purification

The commercial CNTs were purified using a multi-step purification method. After a 2-h thermal treatment at 450 °C in the air to remove amorphous carbon, the remaining solids were sonicated in a 3 M HCl aqueous solution for 1 h, followed by stirring in the HCl solution for another 12 h. The remaining CNTs were then recovered by filtration and washed with DI H_2O until the pH of the filtrate was stable. The recovered CNTs were dried in a vacuum oven at 80 °C and then annealed at 1200 °C for 3 h in a 5% H_2/Ar flow.

FePc/CNT catalyst synthesis

About 20 mg of purified CNTs were dispersed in 10 mL of DMF by bath sonication for 1 h. Another 10 mL DMF solution containing 2 mg of FePc was added to the CNT DMF dispersion under sonication. The mixture was sonicated for 1 h and then stirred at 60 °C for 24 h. Afterward, solid products in the mix were recovered by vacuum filtration, washed with 1 M HCl, DMF, ethanol, and DI water, and dried in a vacuum oven at 80 °C for 24 h.

PPc synthesis

PPc was synthesized by dissolving TCNB (20 mg) and DBU (17.1 mg) at a molar ratio of 1 : 1 in 10 mL of 1-pentanol in an Ar-filled glovebox. After dissolution, the mixture was transferred to a microwave rector (Milestone flexiWAVE microwave platform) and heated at 180 °C for 2.5 h under 800 W

microwave irradiation. The resulting products were recovered by filtration, sequentially washed with 1 M HCl, DMF, ethanol, and DI H_2O, and then dried in a vacuum oven at 80 °C for 24 h. The final PPc production yield was 67.7%.

FePPc synthesis

FePPc was synthesized by dissolving TCNB (20 mg), DBU (17.1 mg), and $FeCl_2$ (7.11 mg) at a molar ratio of 1 : 1 : 0.5 in 10 mL of 1-pentanol in a glovebox. After dissolution, the mixture was transferred to a microwave rector and heated at 180 °C for 2.5 h at 800 W. The resulting products were recovered by filtration, sequentially washed with 1 M HCl, DMF, ethanol, and DI H_2O, and then dried in a vacuum oven at 80 °C for 24 h. The FePPc production yield was 72.3%.

FePPc/CNT catalyst synthesis

The FePPc/CNT catalyst was synthesized using similar conditions to FePPc, except that 20 mg of purified CNTs were dispersed in 1-pentanol (10 mL) by bath sonication before adding the FePPc precursors. After the microwave-assisted solvent-thermal treatment, the resulting products were recovered and treated similar to FePPc.

m-FePPc/CNT catalyst synthesis

The m-FePPc/CNT catalyst was synthesized by physically mixing 10 mg of as-synthesized FePPc with 20 mg of purified CNTs in 20 mL DMF by bath sonication for 30 min, followed by stirring for another 24 h. The solid product was recovered by filtration, washed with DMF and ethanol, and dried in a vacuum oven at 80 °C for 24 h.

Characterization

X-ray diffraction (XRD) patterns of the catalysts were collected on a powder XRD diffractometer (PANalytical X'Pert) with a Cu-Kα source (λ = 1.54178 Å) scanned between a 2θ of 5 and 50° with a scan rate of 5° min^{-1}. N_2 physisorption isotherms were collected on a gas sorption analyzer (Quantachrome Autosorb iQ2). Specific surface areas were calculated from N_2 desorption isotherms using the Brunauer–Emmett–Teller (BET) method. The metal mass loadings in catalysts were measured by digesting in 70% HNO_3 overnight, diluting, and analyzing using inductively coupled plasma mass spectroscopy (ICP-MS, Nexion 350X). Transmission electron microscopy and high-angle annular dark-field scanning transmission electron microscopy (TEM and HAADF-STEM) images were obtained on a microscope (FEI Themis-Z) at 300 kV. Energy-dispersive X-ray spectroscopy (EDX) was used for elemental mappings on the same microscope. The catalysts were dispersed in IPA by 30 min of sonication before drop-casting on Cu TEM grids. X-ray photoelectron spectroscopy (XPS) data were collected on an XPS spectrometer (Thermo Scientific K-Alpha+) with an Al Kα source (1486.3 eV). Ultraviolet–visible (UV-vis) absorption spectra were collected using a spectrometer (Shimadzu UV-3600). X-ray absorption spectroscopy (XAS) was conducted on the MEX-1 Beamline at Australia Synchrotron in a fluorescence mode.

Electrochemical measurements

Electrochemical tests were first carried out in a three-electrode configuration using an electrochemical workstation (CHI 760). A rotary ring-disk electrode (RRDE, E6R1, Pine Instrument, calibrated collection efficiency N = 25%, glassy carbon disk area = 0.19625 cm^2) was used as the working electrode. A graphite rod and an Ag/AgCl (3.0 M KCl filling, Pine Instrument) were used as the counter and reference electrodes, respectively. Before each measurement, the Ag/AgCl reference electrode was calibrated in H_2-saturated 0.5 M H_2SO_4 solution. All reported potentials were converted and referred to the reversible hydrogen electrode (V_{RHE}):

$$E_{RHE} = E_{Ag/AgCl} + 0.0591 \times pH + 0.197 \quad (1)$$

Catalyst ink was prepared by dispersing 5 mg of catalysts in 1 mL water/IPA solution (100 μL of water and 900 μL of IPA) containing 0.05 wt% Nafion 117. The mixture was sonicated for 1 h before being dropped onto the glassy carbon working electrode at a mass loading of 0.2 mg cm^{-2}.

Cyclic voltammetry (CV) was conducted in an Ar-saturated 0.1 M $HClO_4$ electrolyte at a 50 mV s^{-1} scan rate. Linear sweep voltammetry (LSV) polarization curves were obtained in an O_2-saturated 0.1 M $HClO_4$ electrolyte at 25 °C with a rotation rate of 1600 rpm without iR-compensation. The disk electrode current (i_{disk}) was recorded under a potential scan rate of 10 mV s^{-1}, while the ring electrode current (i_{ring}) was collected under a bias of 1.2 V_{RHE}. The faradaic efficiency related to H_2O_2 production ($FE_{H_2O_2}$) and the corresponding electron transfer number (n) were calculated by:

$$FE_{H_2O_2} = 100 \times \frac{i_{ring}/N}{|i_{disk}|} \quad (2)$$

$$n = 4 \times \frac{|i_{disk}|}{|i_{disk}| + i_{ring}/N} \quad (3)$$

The ORR kinetic current density (j_k) was calculated using the Koutechký–Levich equation:

$$\frac{1}{j_{disk}} = \frac{1}{j_L} + \frac{1}{j_k} = \frac{1}{0.62nFC_0D_0^{2/3}\nu^{-1/6}w^{1/2}} + \frac{1}{j_k} \quad (4)$$

where j_{disk}, j_L, and j_k are the measured disk, diffusive limiting and kinetic current density, respectively, n is the electron transfer number, F is the Faraday constant (96 485 C mol^{-1}), C_0 is the concentration of O_2 in the electrolyte (1.2×10^{-3} M), D_0 is the O_2 diffusion coefficient (1.9×10^{-5} cm^2 s^{-1}), ν is the kinetic viscosity of water (0.01 cm^2 s^{-1}), and w is the angular rotation rate.

The turnover frequency (TOF, $site^{-1}$ s^{-1}) of the catalysts was calculated using:

$$TOF = \frac{j_k \times N_A}{\rho \times F \times n \times L} \quad (5)$$

where j_k (mA cm^{-2}) is the kinetic current density, N_A is the Avogadro constant (6.02×10^{23} mol^{-1}), ρ (site g^{-1}) is the single-atom site density determined from nitrite stripping, F is the Faraday constant (96 485 C mol^{-1}), n is the electron transfer

number, and L is the catalyst mass loading on the electrodes (0.2 mg cm^{-2}).

The stability of the catalysts was studied using CV cycling and chronoamperometric tests. CV cycling tests were performed between 0.6 and 1.0 V_{RHE} in the O_2-saturated 0.1 M $HClO_4$ at 50 mV s^{-1} over multiple cycles. LSV curves were recorded before and after the CV cycling. Chronoamperometric tests were performed by depositing catalysts on a gas-diffusion electrode (GDE) at 1 mg cm^{-2}. The catalysts were held at 0.6 V_{RHE} in O_2-saturated 0.1 M $HClO_4$.

Selected catalysts were also assembled into membrane electrode assemblies (MEAs), and their stability was evaluated using a fuel cell. Experimental details are provided in the ESI.†

1,10-Phenanthroline (*o*-phen) colorimetry. An *o*-phen colorimetric method was used to distinguish Fe in the Fe–N_4 structure or free Fe ions in electrolytes.[32,33] $NH_2OH{\cdot}HCl$ was first used to reduce any Fe^{3+} to Fe^{2+} using:

$$4Fe^{3+} + 2NH_2OH{\cdot}HCl \rightarrow 4Fe^{2+} + N_2O + 4H^+ + 2H_2O + 2Cl^- \quad (6)$$

Subsequently, *o*-phen reacted selectively with Fe^{2+}, forming a strongly colored complex with maximum absorption at 510 nm within a pH from 4 to 5 by:

$$Fe^{2+} + 3C_{12}H_8N_2 \rightarrow [Fe(C_{12}H_8N_2)_3]^{2+} \quad (7)$$

The solution pH was controlled using a 0.1 M sodium acetate buffer (pH = 4.6). Standard adsorption curves of Fe^{3+} were prepared using $NH_4Fe(SO_4)_2{\cdot}12H_2O$ and HCl.

Nitrite stripping test. The density of exposed Fe single atom sites was further quantified by a nitrite stripping method following the reactions shown below:[18,34]

$$Fe^{2+}{-}N_4 + NO_2^- + 2H^+ \rightarrow NO{-}Fe^{2+}{-}N_4 + H_2O \quad (8)$$

$$NO{-}Fe^{3+}{-}N_4 + 5e^- + 6H^+ \rightarrow Fe^{3+}{-}N_4 + NH_4^+ + H_2O \quad (9)$$

Electrochemical measurements were conducted using the three-electrode configuration described above, except a 0.5 M sodium acetate buffer (pH = 5.2) was used as the electrolyte. Briefly, ORR LSV curves were collected in Ar- or O_2-saturated electrolytes at 10 mV s^{-1} between 1.0 and 0 V_{RHE} after the catalyst was cycled between 1.1 and −0.45 V_{RHE} at 100 mV s^{-1}. These LSV and CV curves were used as baselines. Afterward, an electrode loaded with catalysts was dipped in a 0.125 M $NaNO_2$ solution for 5 min at the open-circuit potential (V_{OC}) at 300 rpm. The electrode was removed and washed with DI H_2O and a fresh electrolyte at V_{OC} for 5 min. The ORR performance of nitrite-poisoned catalysts was recorded under the same conditions until their ORR performance recovered. The single atom site density (ρ, sites g^{-1}) was calculated using the following equation:

$$\rho = Q \cdot \frac{N_A}{nFvm} \quad (10)$$

where Q (C) is the charge obtained from CV scans, v is the scan rate (V s^{-1}), and m is the mass loading of the catalysts (g). Every nitrite stripping test was conducted at least three times. The results were reproducible.

Theoretical calculations. All spin-polarized density functional theory (DFT) calculations were performed using the Vienna *Ab initio* Simulation Package (VASP) based on the projector augmented wave method.[35] The Kohn–Sham wave functions were expanded in a plane-wave basis set with a cutoff kinetic energy of 520 eV. The generalized gradient approximation method with the revised Perdew–Burke–Ernzerhof (RPBE) functional was used to describe the electron–electron exchange and correlation interactions.[36,37] The van der Waals interaction was described by Grimme's method.[38] The convergence criterion for the electronic self-consistent loop and the residual force of each atom was set to 10^{-5} eV and −0.03 eV $Å^{-1}$, respectively. A vacuum thickness of 15 Å along the *z*-direction was added to avoid the periodic interaction. The Gamma-centered *k*-point set of (2 × 2 × 1) was used to sample the Brillouin zone. The ORR mechanism for water production proceeds *via* a 4-electron pathway involving various reaction intermediates.[39] The analysis of ORR free energy was based on the computational hydrogen electrode method (CHE).[40]

Results and discussion

Catalyst synthesis and characterization

Commercial CNTs were first purified to remove metal residues and amorphous carbon so that these impurities in CNTs do not interfere with catalyst synthesis and their catalytic performance. Several analytical techniques, including TEM (Fig. S1, ESI†), XPS (Fig. S2, ESI†), TGA (Fig. S3, ESI†), and EDX (Fig. S4, ESI†), confirmed the removal of the impurities. ICP-MS analysis indicated that Fe residues in purified CNTs were 4 ± 1 ppb. The purified CNTs displayed negligible catalytic activity for the ORR in an acidic 0.1 M $HClO_4$ electrolyte (Fig. S5, ESI†).

Fig. 1a illustrates the synthesis of the FePPc/CNT, FePc/CNT, and m-FePPc/CNT catalysts. FePPc/CNT was synthesized using a microwave-assisted solvent-thermal method (see details in the Experimental section). TCNB reacted with $FeCl_2$ in 1-pentanol under microwave irradiation to form FePPc. In the presence of purified CNTs, the *in situ* FePPc polymerization occurred around CNTs, resulting in core–shell structured FePPc/CNT with a uniform, thin FePPc surrounding individual CNT. FePc/CNT was synthesized by directly adsorbing FePc molecules on purified CNTs. Furthermore, FePPc was also synthesized without CNTs and then physically mixed with purified CNTs to yield m-FePPc/CNT as a reference catalyst. Bright-field TEM images of the catalysts are compared in Fig. 1b. A shell layer on the CNT surfaces is displayed in FePPc/CNT (magnified TEM image of FePPc/CNT in Fig. S6, ESI†). FePc/CNT (mid panel of Fig. 1b) exhibits a morphology similar to pristine CNTs. FePPc aggregates on CNTs are shown in m-FePPc/CNT (bottom panel of Fig. 1b).

HAADF-STEM images of these catalysts (Fig. 1c) show bright dots from single Fe atoms in FePc moieties. EDX elemental mappings (Fig. 1d and Fig. S7, ESI†) show uniform distributions

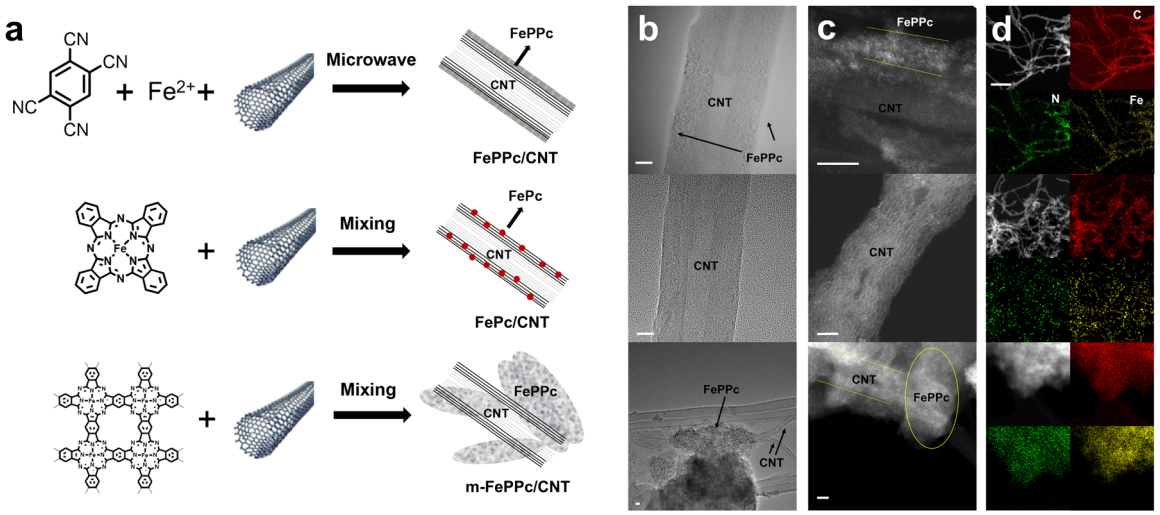

Fig. 1 Synthesis and characterization of FePPc/CNT, FePc/CNT, and m-FePPc/CNT catalysts. (a) Schematic illustration of the catalyst synthesis. (b) TEM, (c) HAADF-STEM, and (d) STEM-EDX images and elemental mappings of FePPc/CNT (top panels), FePc/CNT (mid panels), and m-FePPc/CNT (bottom panels). The scale bars are 5 nm in (b) and (c) and 100 nm in (d).

of C, N, and Fe elements. XAS analysis results indicate that Fe atoms in these catalysts have the same first-shell coordination of 4 and are in similar Fe–N_4 atomic structures (Fig. S8 and Table S2, ESI†). However, the density of bright Fe dots observed in polymer shells of FePPc/CNT and FePPc aggregates of m-FePPc/CNT is much higher than that in FePc/CNT, which collaborate with the Fe mass loadings in these catalysts quantified by ICP-MS. The Fe mass loadings in FePPc/CNT (2.92 wt%) and m-FePPc/CNT (3.24 wt%) are nearly four times that in FePc/CNT (0.80 wt%). In contrast, nitrite stripping test results indicate that the Fe site density in these catalysts is comparable, *i.e.*, 1.11×10^{20}, 1.31×10^{20}, and 7.14×10^{19} sites g^{-1}, for FePPc/CNT, m-FePPc/CNT, and FePc/CNT catalysts, respectively (Table S3, ESI†), which can be translated into Fe mass loadings of FePPc/CNT (1.03 wt%), m-FePPc/CNT (1.22 wt%), and FePc/CNT (0.66 wt%). The differences in the Fe site density detected by ICP-MS and nitrite stripping suggest that only a fraction of Fe sites in FePPc/CNT and m-FePPc/CNT (about 30%) are directly exposed to electrolytes, and others may have been embedded in FePPc.

High-resolution XPS spectra collected in these catalysts' Fe 2p, N 1s, and C 1s regions are identical (Fig. S9a, ESI†). Their Fe 2p spectra exhibit two peaks at 710.0 and 723.2 eV, corresponding to the spin–orbital split Fe $2p_{3/2}$ and Fe $2p_{1/2}$, respectively.[41,42] Their N 1*s* spectra were deconvoluted into two peaks at 399.5 and 398.9 eV with comparable peak areas, which can be assigned to the Fe–N and –C═N– bonds in FePc moieties, respectively.[30,43,44] Furthermore, their C 1*s* spectra show a main peak at 284.4 eV, corresponding to the sp^2-hybridized graphitic carbon in CNTs. The other C 1s peak at 285.4 eV can be assigned to C–N bonds in FePc and FePPc.[30] The Raman spectra of these catalysts are similar (Fig. S9, ESI†), showing *D* (~1320 cm^{-1}) and *G* (~1580 cm^{-1}) bands from CNTs with a comparable intensity. Their XRD patterns (Fig. S9c, ESI†) exhibit a strong graphite (002) peak at a 2θ of ~25°. However, no obvious diffraction peaks from the (002) lattice of FePPc can be identified in FePPc/CNT and m-FePPc/CNT, indicating the amorphous nature of FePPc. The specific surface areas of these catalysts determined by N_2 physisorption are similar to that of purified CNTs, ranging from 160 to 170 $m^2\ g^{-1}$ (Table S3 and Fig. S9d, ESI†). In short, the comprehensive catalyst characterization indicates that FePPc/CNT, FePc/CNT, and m-FePPc/CNT contain similar Fe–N_4 sites in FePc moieties, and the density of their Fe sites exposed to electrolytes is also comparable.

ORR activity assessment

ORR catalytic activities of FePPc/CNT, FePc/CNT, and m-FePPc/CNT catalysts were first compared in the O_2-saturated acidic 0.1 M $HClO_4$ electrolyte using catalyst-deposited RRDEs. $HClO_4$ can reversibly poison active sites, which is more reliable for electrochemical tests among common acidic electrolytes.[45,46] Fig. 2a displays LSV curves recorded at a scan rate of 10 mV s^{-1} without the iR-compensation at a rotational speed of 1600 rpm. The ORR disk onset potential (defined as the potential required to reach a disk current density of 0.025 mA cm^{-2}) of FePPc/CNT and m-FePPc/CNT is 0.87 and 0.84 V_{RHE}, which are higher than that of FePc/CNT at 0.76 V_{RHE}. Besides, FePPc/CNT exhibits a higher half-wave potential ($E_{1/2}$) at 0.74 V_{RHE} than m-FePPc/CNT (0.66 V_{RHE}) and FePc/CNT (0.61 V_{RHE}). FePPc/CNT also shows a 65% higher diffusive limiting current density (j_L) over that of m-FePPc/CNT, along with the lowest H_2O_2 faradaic efficiency ($FE_{H_2O_2}$) of 1.2% at 0.3 V_{RHE}, showing excellent ORR catalytic activity and selectivity (Fig. 2b).

The Tafel slopes of these catalysts were calculated from their ORR kinetic current density obtained by the Koutechký–Levich equation. FePPc/CNT demonstrates superior kinetic performance with a lowest Tafel slope of 51 mV dec^{-1} compared to 69 mV dec^{-1} of FePc/CNT and 117 mV dec^{-1} of m-FePPc/CNT (Fig. 2c). The smaller Tafel slopes of FePPc/CNT and FePc/CNT

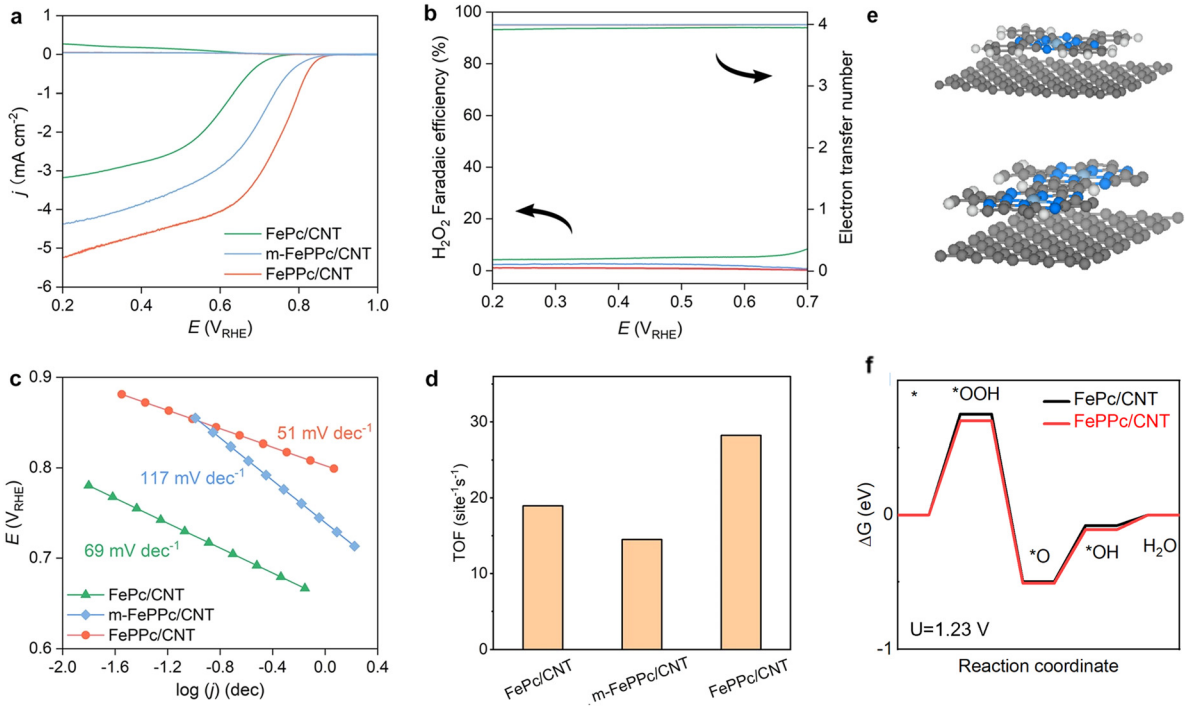

Fig. 2 ORR catalytic activity of FePPc/CNT, FePc/CNT, and m-FePPc/CNT catalysts. (a) LSV polarization curves measured at 1600 rpm in an O_2-saturated 0.1 M $HClO_4$ electrolyte with a scan rate of 10 mV s^{-1}, and (b) the corresponding $FE_{H_2O_2}$ and electron transfer number (*n*). (c) Tafel plots and the (d) TOF at 0.6 V_{RHE}. (e) Atomistic models of FePc/CNT (top) and FePPc/CNT (bottom) used in DFT calculations. A periodic unit lattice extracted from the FePPc structure is presented. (f) Calculated ORR free energy diagrams for FePc/CNT and FePPc/CNT.

suggest that forming the OOH* intermediate is the rate-limiting step of the ORR. In contrast, the higher Tafel slope of m-FePPc/CNT indicates that the rate-limiting step changes to the electron transfer in the $*O_2^-$ formation ($* + O_2 + e^- \rightarrow *O_2^-$).[47] This change was also revealed by electrochemical impedance spectroscopy. Nyquist plots of these catalysts at the same current density (0.6 V_{RHE}) show that FePPc/CNT (20.1 Ohm) and FePc/CNT (30.7 Ohm) have a smaller R_{CT} than m-FePPc/CNT (24.3 Ohm, Fig. S10, ESI†). The close interactions between the FePPc shell and CNTs or between FePc molecules with CNTs enable more efficient electron transfer than FePPc deposited on CNTs. The intrinsic catalytic activity of Fe–N_4 sites of these catalysts was compared by their TOF at 0.6 V_{RHE}. TOF calculations were based on the Fe active site density determined by the nitrite stripping method. Fig. 2d shows that FePPc/CNT exhibits the highest TOF of 0.98 $site^{-1}$ s^{-1}, much higher than that of FePc/CNT (0.22 $site^{-1}$ s^{-1}) and m-FePPc/CNT (0.30 $site^{-1}$ s^{-1}), indicating superior intrinsic catalytic activity.

ORR free energy on active sites of FePc/CNT and FePPc/CNT was determined by DFT calculations. The atomic models of the active sites and adsorbed reaction intermediates along the $4e^-$-ORR pathway are displayed in Fig. 2e and Fig. S11 (ESI†). The atomic models are created by placing a layer of FePc or FePPc on a graphene sheet. Fig. 2f displays the calculated free-energy ORR diagrams (also listed in Table S4, ESI†). FePc/CNT has a slightly larger barrier than FePPc/CNT in the formation of *OOH, which is RDS for the ORR. DFT results suggest that FePPc/CNT may outperform FePc/CNT because its polymerized macrocycle pulls just enough electrons away from its Fe–N_4 centers to weaken the binding to *O(H) intermediates, shrinking the energy span of the ORR cycle and lowering the theoretical overpotential. The theoretical results suggest that FePPc/CNT would have more active sites with improved intrinsic catalytic activity for the ORR.

ORR stability

Next, the stability of FePc/CNT, m-FePPc/CNT, and FePPc/CNT for the ORR in acidic electrolytes was compared. First, CV cycling tests were performed in a three-electrode configuration between 0.6 and 1.0 V_{RHE} in an O_2-saturated 0.1 M $HClO_4$ electrolyte at 50 mV s^{-1}. Fig. 3a shows LSV curves collected before and after 1000 cycles. FePc/CNT exhibits the most significant performance degradation, with its onset potential and $E_{1/2}$ reducing from 0.76 to 0.58 V_{RHE} (Δ = 180 mV) and 0.61 to 0.46 V_{RHE} (Δ = 150 mV), respectively. In contrast, m-FePPc/CNT and FePPc/CNT showed better stability, exhibiting a smaller onset potential and $E_{1/2}$ shifts (Fig. 3b). Specifically, FePPc/CNT exhibits the smallest onset potential and $E_{1/2}$ shifts by 100 and 103 mV, respectively.

Next, the intrinsic activity changes of these catalysts before and after the CV cycling tests were quantified using their TOF values. The nitrite stripping method first quantified the Fe active site density before and after the CV cycling tests (Fig. S12, ESI†). FePc/CNT and FePPc/CNT exhibit a similar loss of 33.2% and 47.2% of the Fe active site density, respectively

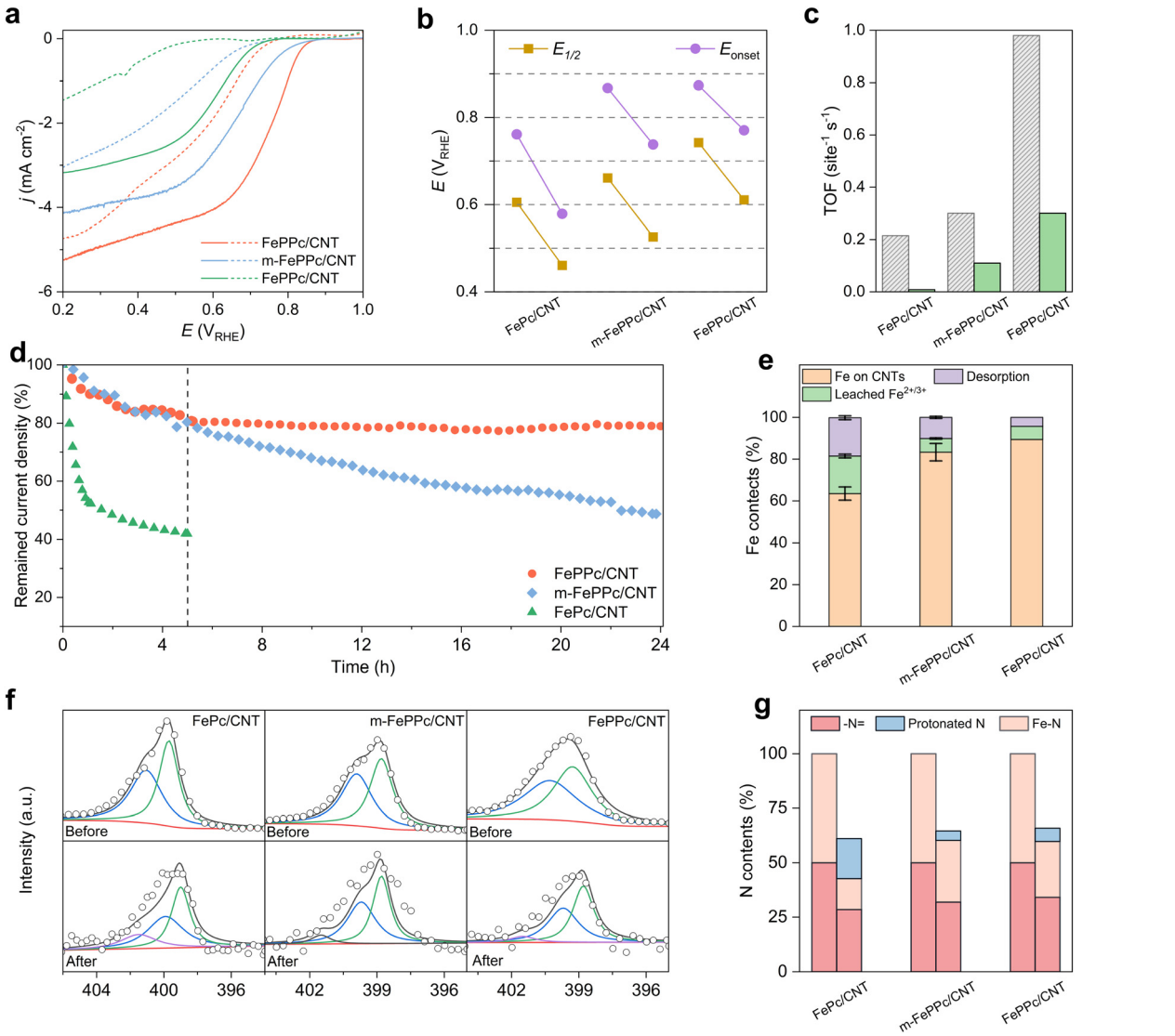

Fig. 3 ORR stability of FePPc/CNT, FePc/CNT, and m-FePPc/CNT catalysts. (a) LSV curves before and after 1000 CV cycles scanned between 0.6 and 1.0 V_{RHE} in the O_2-saturated 0.1 M $HClO_4$ electrolyte. (b) Changes of $E_{1/2}$ and the onset potential, and (c) changes of the TOF before and after CV cycling. (d) ORR chronoamperometric performance over 24 h in the 0.1 M $HClO_4$ electrolyte at 0.6 V_{RHE}. Characterization of FePPc/CNT, FePc/CNT, and m-FePPc/CNT catalysts after 5 h of chronoamperometric stability tests: (e) the mass distribution of Fe species in leached free $Fe^{2+/3+}$ in electrolytes (green color), desorbed FePc molecules or FePPc fragments in electrolytes (purple color), and Fe remained on CNTs (orange color); (f) N 1*s* XPS spectra of catalysts before (top) and after (bottom) the chronoamperometric stability test; and (g) the distribution of different N species.

(Table S5, ESI†), much less than the 56.3% of m-FePPc/CNT, indicating that FePPc in m-FePPc/CNT is prone to detachment from CNTs. The TOF values before and after the CV cycling test are compared in Fig. 3c. The TOF of FePc/CNT drops from 0.22 to 0.01 site^{-1} s^{-1}, losing most of its activity. Similarly, the TOF of m-FePPc/CNT decreases from 0.30 to 0.11 site^{-1} s^{-1}. In contrast, FePPc/CNT has the highest initial TOF of 0.98 site^{-1} s^{-1}, decreasing to 0.32 site^{-1} s^{-1}. These results suggest significant differences in the degradation mechanisms of these catalysts.

Their stability was further evaluated using chronoamperometric tests in the 0.1 M $HClO_4$ electrolyte at 0.6 V_{RHE} over 24 h. Fig. 3d shows that FePc/CNT deactivates rapidly, losing ~50% of its initial current density after 1.5 h and retaining only 42% after 5 h. m-FePPc/CNT shows better stability, losing ~17% of its initial current density after 3 h and retaining ~49% after 24 h. FePPc/CNT demonstrates much better stability, losing similarly ~17% of its initial current density after 3 h but retaining ~80% after 24 h.

After 5 h of chronoamperometric stability tests, these catalysts were characterized to compare their structural changes. The Fe concentration in electrolytes was quantified using ICP-MS. Fig. 3e and Table S6 (ESI†) show that FePc/CNT leaches around 36.5%/0.29 wt% of Fe to the acidic electrolyte, indicating poor stability. In contrast, FePPc/CNT and m-FePPc/CNT leached only 10.6%/0.31 wt% and 16.7%/0.54 wt%, respectively, indicating that incorporating Fe–N_4 active sites into FePPc polymeric structures effectively inhibits Fe leaching. Next, the

o-phen colorimetric method was used to distinguish two types of leached Fe species in electrolytes: free $Fe^{2+/3+}$ and Fe in Fe–N_4 structures in detached FePc molecules or FePPc fragments (see details in the Experimental section, Fig. S13 and Table S6, ESI†). Nearly 18.1% of the leached Fe (0.14 wt%) from FePc/CNT is free $Fe^{2+/3+}$, and the other half (18.4%/0.15 wt%) is in detached FePc molecules from CNTs. m-FePPc/CNT and FePPc/CNT show lower free $Fe^{2+/3+}$ leaching levels (6.6%/0.21 wt%; 6.3%/0.18 wt%), indicating that Fe–N bonds in FePPc are more stable than those in FePc molecules. The fraction of detached FePPc fragments from m-FePPc/CNT is much higher than that from FePPc/CNT (10.1%/0.33 wt% *vs.* 4.3%/0.13 wt%), indicating that the core–shell structure of FePPc/CNT induces strong interactions between FePPc and CNTs than the physically mixed m-FePPc/CNT. FePPc/CNT has the lowest total Fe loss and fewer detached FePPc fragments, indicating that incorporating catalytically active Fe–N_4 sites into the FePPc shell around CNTs can improve catalyst stability.[30,48]

The N 1s XPS spectra (Fig. 3f) of these catalysts before and after the 5 h chronoamperometric stability tests were also compared to evaluate the changes in their Fe coordination environment. The deconvolution of the N 1s XPS spectra shows that the abundance ratio between imine (–C═N–) and Fe–N in the catalysts before the stability tests is 1 : 1 (Fig. 3g), consistent with their theoretical molecular structures. After the stability test, new peaks at 401.4 eV emerged from protonated N (–N–-H). This peak is most prominent in FePc/CNT, accounting for 18.4% of total N (Table S7, ESI†). Meanwhile, it only accounts for 6.1% of N in FePPc/CNT and 4.3% of m-FePPc/CNT, correlating with their lower $FE_{H_2O_2}$. This can be attributed to the fact that H_2O_2 produced from the ORR would generate intermediates to attack Fe–N_4 sites, leading to Fe leaching. More Fe leaching results in structural defects, making N atoms more susceptible to hydrogenation and subsequent protonation.

Self-renewal mechanism of FePPc/CNT

Although FePPc/CNT exhibits better stability than m-FePPc/CNT and FePc/CNT, a detailed analysis of their degradation behavior in a 48 h chronoamperometric stability test reveals a unique behavior. Unlike the rapid and continuous degradation of FePc/CNT and m-FePPc/CNT (Fig. 3a), the catalytic activity of FePPc/CNT declines in the first 5 h, followed by a period with relatively stable activity for the next 19 h with only 3% reduction in the current density. The catalytic activity only declines significantly after 25.6 h (Fig. 4a). Surprisingly, small catalytic activity increments appear during the relatively stable period at different times, for example, a 0.5% increase in the current density at 13–13.5 h and another similar increase at 23 h (see several enlarged boxes in Fig. 4a).

The distribution of Fe species leached in the electrolytes and retained on FePPc/CNT was analyzed after 5, 10, 24, and 48 h of the chronoamperometric stability test to understand this unique behavior. Fig. 4b and Table S6 (ESI†) show that Fe continuously leaches into electrolytes, primarily free $Fe^{2+/3+}$ (green color bars). Leached free $Fe^{2+/3+}$ increases from 6.3%/0.18 wt% after 5 h to 16.8%/0.49 wt% after 24 h and 37.6%/1.1 wt% after 48 h. Similarly, Fig. 4b also displays that the abundance of leached Fe in FePPc fragments (purple color bars) increases predominantly in the first 5 h, accounting for 4.3%/0.13 wt% Fe in FePPc/CNT. Leached Fe in FePPc fragments also continuously increases to 5.0%/0.15 wt% at 10 h and 8.1%/0.24 wt% at 24 h before reaching 10.7%/0.31 wt% at 48 h. The fast initial loss can be attributed to the initial detachment of FePPc fragments that are weakly attached to the catalyst surfaces. Then, the relatively stable FePPc shell on CNTs still detaches moderately yet continuously from CNTs. The continuous increase in the abundance of leached Fe species in electrolytes disagrees with their relatively stable catalytic activity shown in Fig. 4a, which cannot explain the small catalytic activity increments observed.

Next, nitrite stripping tests were conducted to quantify Fe sites retained on FePPc/CNT. Fig. S14 and Table S5 (ESI†) indicate a 45.8% loss of the Fe site density within the first 5 h from 1.11×10^{20} sites g^{-1} to 6.02×10^{19} sites g^{-1}, and 52.5% to 5.27×10^{19} sites g^{-1} after 10 h. However, from 10 to 24 h, the Fe site density slightly increases from 5.27×10^{19} to 5.88×10^{19} sites, which matches the observed catalytic activity changes. The Fe site density declines only after 25.6 h.

Based on the above observations, we propose that the unique degradation behavior of FePPc/CNT comes from the layer-by-layer shedding of FePPc fragments from the FePPc shell on CNTs, which exposes fresh FePPc layers underneath the shed FePPc surface. When fresh FePPc surfaces are exposed, they provide new Fe–N_4 catalytically active sites for the ORR. This explains why the abundance of leached Fe species in electrolytes continuously increases while the Fe site density remains relatively constant from 10 to 24 h. The self-renewed catalyst surfaces enable stable catalytic activity up to 25.6 h, as displayed in Fig. 4a. The exposure to large areas of fresh FePPc surfaces also contributes to the minor increases in the current density at different times. The catalytic activity only declines when all fresh surfaces are exhausted after 25.6 h.

A detailed TEM analysis of FePPc/CNT was conducted after the stability tests to support the hypothesis. Fig. 4c shows that the thickness of the ordered FePPc shell on CNTs decreases from the initial 2.3 to 1.61 nm at 5 h, 0.97 nm at 10 h, and 0.46 nm at 24 h, indicating the shedding of FePPc layers from the shell. Shedding top FePPc layers would expose new FePPc surfaces underneath with fresh Fe–N_4 sites for the ORR. At the same time, disordered FePPc aggregates emerge on some areas of CNT surfaces, with the thickness gradually increasing from 2.3 nm initially to 2.92 nm at 5 h, 3.24 nm at 10 h, and 5.62 nm at 24 h (Fig. 4d). They are likely from the sedimentation of shed FePPc fragments. In the HAADF-STEM images of the sample after the 24-h test, we also observe ''shedding'' and ''sedimenting'' taking place on a single CNT (Fig. 4e and Fig. S15, ESI†), indicating that the two degradation phenomena happen simultaneously.

Furthermore, HAADF-STEM images (Fig. 4f) and the corresponding EDX analyses (Fig. S16 and S17, ESI†) of individual CNTs in FePPc/CNT show many bright spots identified as FeO_x nanoclusters. This observation is consistent with a previous study.[49] As the ORR progressed from 5 to 48 h, the average size

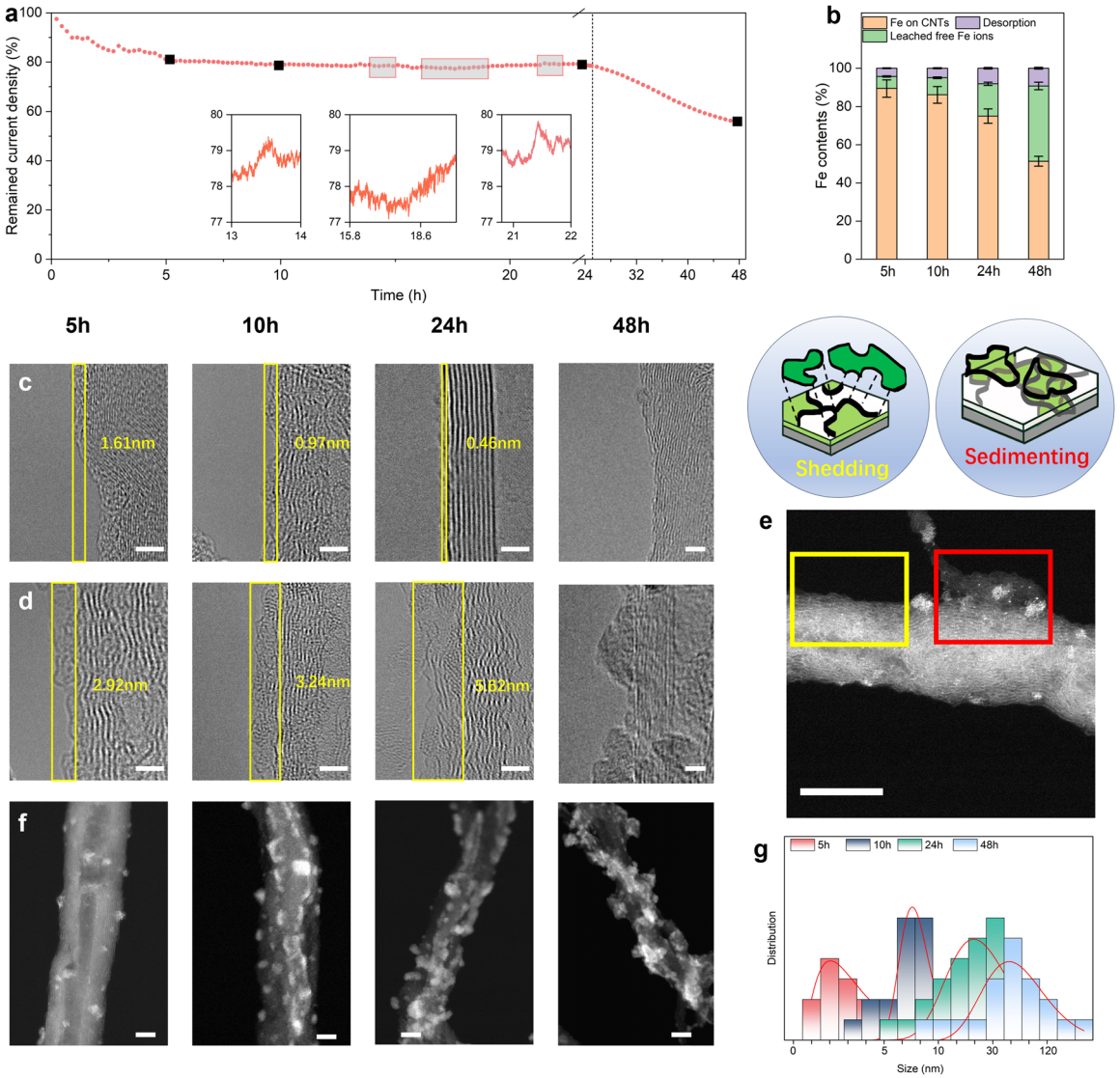

Fig. 4 Self-renewal mechanism of the FePPc/CNT catalyst. (a) An extended ORR chronoamperometric stability test over 48 h. The shaded red frames are enlarged for detailed comparison. (b) The mass distribution of Fe species in leached free $Fe^{2+/3+}$ in electrolytes (green color), desorbed FePPc fragments in electrolytes (purple color), and Fe that remained on CNTs (orange color) after 5, 10, 24, and 48 h stability tests. The corresponding HR-TEM images of FePPc/CNT (the diameter measurement was done in Velox. The scale bars are 2 nm): (c) the continuous shedding of the FePPc shell from CNTs and the (d) sediments of FePPc fragments on CNTs. (e) A schematic illustration (top) and an HR-TEM image of one single CNT (bottom) with ''shedding'' and ''sedimenting'' taking place simultaneously (the scale bar is 10 nm; reaction time is 24 h). (f) HAADF-STEM images (scale bars are 5 nm) of FeO_x particles observed on CNTs after 5, 10, 24, and 48 h stability tests and (g) the corresponding size distribution of FeO_x particles.

of FeO_x nanoclusters increased significantly, as summarized in Fig. 4g and Table S7 (ESI†). About 16 FeO_x nanoclusters, with an average area of 2.28 nm^2 and the largest size of 5.24 nm^2, are observed on a 50 nm long CNT after 5 h of the stability test. By 10 h, their average size grows to 4.87 nm^2, with the largest cluster reaching 19.97 nm^2. After 24 and 48 h, FeO_x clusters further aggregate, and their morphology also shifts from spherical to more irregular, and the average particle size increases to 35.53 nm^2. The growth in the size of FeO_x nanoclusters indicates that leached $Fe^{2+/3+}$ migrate on CNT surfaces and aggregate to larger nanoclusters, which contributes to the permanent loss of catalytic activity over time.

FePPc/CNT MEA stability test

We also tested the stability of FePPc/CNT in MEA over 5000 CV cycles, following a standard protocol.[50] Experimental details are described in the ESI,† and the photos of the FePPc/CNT MEA and the assembled full hydrogen full cell are shown in Fig. S18 (ESI†). The polarization curves before and after the cycling are shown in Fig. S19 (ESI†). Before cycling, the cell achieves a maximum current density of around 1.4 A cm^{-2} with a peak power density of approximately 0.32 W cm^{-2}. After cycling, the maximum current density dropped to about 0.9 A cm^{-2}, and the peak power density decreased significantly to roughly 0.20 W cm^{-2}, indicating a ~37.5% loss in power output.

The catalysts after cycling were examined using HAADF (Fig. S20, ESI†), displaying morphologies consistent with those observed in earlier stability tests. These results underscore the need for enhanced catalyst stability.

Conclusions

Incorporating Fe–N_4 sites into the FePPc polymeric structure increases the Fe mass loading significantly from 0.80 wt% for FePc/CNT to 2.92 wt% for FePPc/CNT, compared to directly depositing FePc molecules on CNTs. Despite the higher Fe mass loading, the density of Fe–N_4 sites directly exposed to the electrolyte remains comparable ($7.14–11.1 \times 10^{19}$ sites g^{-1}). FePPc/CNT exhibits enhanced catalytic performance in the 0.1 M $HClO_4$ electrolyte, as evidenced by a higher half-wave potential ($E_{1/2}$ = 0.74 V_{RHE}) compared to m-FePPc/CNT (0.66 V_{RHE}) and FePc/CNT (0.61 V_{RHE}). Furthermore, FePPc/CNT demonstrates the lowest Tafel slope (51 mV dec^{-1}), outperforming FePc/CNT (69 mV dec^{-1}) and m-FePPc/CNT (117 mV dec^{-1}), and achieves the highest TOF of 0.98 site^{-1} s^{-1}, significantly surpassing that of FePc/CNT (0.22 site^{-1} s^{-1}) and m-FePPc/CNT (0.30 site^{-1} s^{-1}). DFT results suggest that polymerized macrocycles pull electrons from Fe–N_4 centers to enhance their intrinsic catalytic activity. Moreover, FePPc/CNT exhibits superior operational stability, retaining approximately 80% of its initial current density after 24 h of 0.1 M $HClO_4$, in contrast to m-FePPc/CNT (~49% after 24 h) and FePc/CNT (~42% after just 5 h). Quantitative analysis of Fe species leached into the electrolyte and deposited on CNTs reveals that FePPc/CNT has a unique self-renewal mechanism. It involves layer-by-layer shedding and sedimentation of FePPc fragments from the polymeric shell. The shedding process exposes fresh FePPc surfaces with new Fe–N_4 active sites, thereby sustaining catalytic activity. However, sedimented FePPc fragments redeposit as disordered aggregates on CNTs. Leached Fe^{2+}/Fe^{3+} species also migrate along CNT surfaces and subsequently form FeO_x nanoclusters, contributing to irreversible deactivation. These findings provide several valuable insights into the structural and mechanistic design principles of active and stable heterogeneous molecular M–N–C catalysts: (1) incorporating Fe–N_4 sites into polymeric structures is beneficial to increase their stability; (2) forming a close interaction between polymeric structures and carbon substrates can improve the catalytic activity; and (3) the layer-by-layer shedding process of shell structures can offer a self-renewable catalyst surface to enable extended stable catalytic activity.

Conflicts of interest

There are no conflicts to declare.

Data availability

The data supporting this article have been included as part of the ESI.†

Acknowledgements

This work is financially supported by the Australian Research Council (DP230101694 and FT210100218), the ARC Centre of Excellence for Green Electrochemical Transformation of Carbon Dioxide (CE230100017), and the JSPS KAKENHI (JP23K13703). Z. G. acknowledges the Postdoctoral Fellowship Program of CPSF under the Grant Number (GZC20241472). H. L. and L. W. acknowledge the computational resources provided by the Center for Computational Materials Science, Institute for Materials Research, Tohoku University (MASAMUNE-IMR, 202312 SCKXX-0203), the Institute for Solid State Physics (ISSP) at the University of Tokyo, and the National Computational Infrastructure (NCI, NCMAS-2024-59 and NCMAS-2025-157). This research was undertaken on the MEX-1 beamline at the Australian Synchrotron, part of ANSTO.

References

1 A. A. Gewirth and M. S. Thorum, *Inorg. Chem.*, 2010, **49**, 3557–3566.
2 A. A. Gewirth, J. A. Varnell and A. M. DiAscro, *Chem. Rev.*, 2018, **118**, 2313–2339.
3 Z. Chen, D. Higgins, A. Yu, L. Zhang and J. Zhang, *Energy Environ. Sci.*, 2011, **4**, 3167–3192.
4 H. T. Chung, D. A. Cullen, D. Higgins, B. T. Sneed, E. F. Holby, K. L. More and P. Zelenay, *Science*, 2017, **357**, 479–484.
5 V. R. Stamenkovic, B. Fowler, B. S. Mun, G. Wang, P. N. Ross, C. A. Lucas and N. M. Marković, *Science*, 2007, **315**, 493–497.
6 H. A. Gasteiger and N. M. Marković, *Science*, 2009, **324**, 48–49.
7 Y. Zeng, C. Li, B. Li, J. Liang, M. J. Zachman, D. A. Cullen, R. P. Hermann, E. E. Alp, B. Lavina, S. Karakalos, M. Lucero, B. Zhang, M. Wang, Z. Feng, G. Wang, J. Xie, D. J. Myers, J.-P. Dodelet and G. Wu, *Nat. Catal.*, 2023, **6**, 1215–1227.
8 H. Xie, X. Xie, G. Hu, V. Prabhakaran, S. Saha, L. Gonzalez-Lopez, A. H. Phakatkar, M. Hong, M. Wu, R. Shahbazian-Yassar, V. Ramani, M. I. Al-Sheikhly, D.-E. Jiang, Y. Shao and L. Hu, *Nat. Energy*, 2022, **7**, 281–289.
9 Q. Zhang, K. Mamtani, D. Jain, U. Ozkan and A. Asthagiri, *J. Phys. Chem. C*, 2016, **120**, 15173–15184.
10 G. Zhang, Y. Jia, C. Zhang, X. Xiong, K. Sun, R. Chen, W. Chen, Y. Kuang, L. Zheng, H. Tang, W. Liu, J. Liu, X. Sun, W.-F. Lin and H. Dai, *Energy Environ. Sci.*, 2019, **12**, 1317–1325.
11 T. Zhao, J. Wang, Y. Wei, Z. Zhuang, Y. Dou, J. Yang, W.-H. Li and D. Wang, *Energy Environ. Sci.*, 2025, **18**, 3462–3501.
12 Y. Wu, X. Tang, K. Yuan and Y. Chen, *Energy Environ. Sci.*, 2023, **16**, 5663–5687.
13 M. Lefèvre, E. Proietti, F. Jaouen and J.-P. Dodelet, *Science*, 2009, **324**, 71–74.
14 G. Chen, Y. An, S. Liu, F. Sun, H. Qi, H. Wu, Y. He, P. Liu, R. Shi, J. Zhang, A. Kuc, U. Kaiser, T. Zhang, T. Heine, G. Wu and X. Feng, *Energy Environ. Sci.*, 2022, **15**, 2619–2628.

15 Y.-F. Guo, S. Zhao, N. Zhang, Z.-L. Liu, P.-F. Wang, J.-H. Zhang, Y. Xie and T.-F. Yi, *Energy Environ. Sci.*, 2024, **17**, 1725–1755.
16 H. Zhang, S. Hwang, M. Wang, Z. Feng, S. Karakalos, L. Luo, Z. Qiao, X. Xie, C. Wang, D. Su, Y. Shao and G. Wu, *J. Am. Chem. Soc.*, 2017, **139**, 14143–14149.
17 X. Wan, Q. Liu, J. Liu, S. Liu, X. Liu, L. Zheng, J. Shang, R. Yu and J. Shui, *Nat. Commun.*, 2022, **13**, 2963.
18 A. Mehmood, M. Gong, F. Jaouen, A. Roy, A. Zitolo, A. Khan, M.-T. Sougrati, M. Primbs, A. M. Bonastre, D. Fongalland, G. Drazic, P. Strasser and A. Kucernak, *Nat. Catal.*, 2022, **5**, 311–323.
19 H. A. Miller, M. Bellini, W. Oberhauser, X. Deng, H. Chen, Q. He, M. Passaponti, M. Innocenti, R. Yang, F. Sun, Z. Jiang and F. Vizza, *Phys. Chem. Chem. Phys.*, 2016, **18**, 33142–33151.
20 S. Yang, Y. Yu, X. Gao, Z. Zhang and F. Wang, *Chem. Soc. Rev.*, 2021, **50**, 12985–13011.
21 R. Chen, H. Li, D. Chu and G. Wang, *J. Phys. Chem. C*, 2009, **113**, 20689–20697.
22 R. Cao, R. Thapa, H. Kim, X. Xu, M. Gyu Kim, Q. Li, N. Park, M. Liu and J. Cho, *Nat. Commun.*, 2013, **4**, 2076.
23 Z. Zhang, M. Dou, J. Ji and F. Wang, *Nano Energy*, 2017, **34**, 338–343.
24 W. Li, A. Yu, D. C. Higgins, B. G. Llanos and Z. Chen, *J. Am. Chem. Soc.*, 2010, **132**, 17056–17058.
25 S. Baranton, C. Coutanceau, C. Roux, F. Hahn and J. M. Léger, *J. Electroanal. Chem.*, 2005, **577**, 223–234.
26 Y. Shao, J.-P. Dodelet, G. Wu and P. Zelenay, *Adv. Mater.*, 2019, **31**, 1807615.
27 E. F. Holby, G. Wang and P. Zelenay, *ACS Catal.*, 2020, **10**, 14527–14539.
28 K. Kumar, L. Dubau, M. Mermoux, J. Li, A. Zitolo, J. Nelayah, F. Jaouen and F. Maillard, *Angew. Chem., Int. Ed.*, 2020, **59**, 3235–3243.
29 Y. He, S. Liu, C. Priest, Q. Shi and G. Wu, *Chem. Soc. Rev.*, 2020, **49**, 3484–3524.
30 S. Yuan, J. Peng, Y. Zhang, D. J. Zheng, S. Bagi, T. Wang, Y. Román-Leshkov and Y. Shao-Horn, *ACS Catal.*, 2022, **12**, 7278–7287.
31 X. Li and Z. Xiang, *Nat. Commun.*, 2022, **13**, 57.
32 A. E. Harvey Jr, J. A. Smart and E. S. Amis, *Anal. Chem.*, 1955, **27**, 26–29.
33 Y. Yao, L. Lai, Z. Yu, Y. Pan, Y. Yu, V. Lo, A. Roy, B. Chivers, X. Zhong, L. Wei and Y. Chen, *J. Hazard. Mater.*, 2022, **437**, 129328.
34 L. Jiao, J. Li, L. L. Richard, Q. Sun, T. Stracensky, E. Liu, M. T. Sougrati, Z. Zhao, F. Yang, S. Zhong, H. Xu, S. Mukerjee, Y. Huang, D. A. Cullen, J. H. Park, M. Ferrandon, D. J. Myers, F. Jaouen and Q. Jia, *Nat. Mater.*, 2021, **20**, 1385–1391.
35 P. E. Blöchl, *Phys. Rev. B:Condens. Matter Mater. Phys.*, 1994, **50**, 17953–17979.
36 G. Kresse and J. Furthmüller, *Phys. Rev. B:Condens. Matter Mater. Phys.*, 1996, **54**, 11169–11186.
37 B. Hammer, L. B. Hansen and J. K. Nørskov, *Phys. Rev. B:Condens. Matter Mater. Phys.*, 1999, **59**, 7413–7421.
38 S. Grimme, S. Ehrlich and L. Goerigk, *J. Comput. Chem.*, 2011, **32**, 1456–1465.
39 M. Shao, Q. Chang, J.-P. Dodelet and R. Chenitz, *Chem. Rev.*, 2016, **116**, 3594–3657.
40 J. K. Nørskov, J. Rossmeisl, A. Logadottir, L. Lindqvist, J. R. Kitchin, T. Bligaard and H. Jónsson, *J. Phys. Chem. B*, 2004, **108**, 17886–17892.
41 Y. Luo, Y. Chen, Y. Xue, J. Chen, G. Wang, R. Wang, M. Yu and J. Zhang, *Small*, 2022, **18**, 2105594.
42 K.-M. Zhao, S. Liu, Y.-Y. Li, X. Wei, G. Ye, W. Zhu, Y. Su, J. Wang, H. Liu, Z. He, Z.-Y. Zhou and S.-G. Sun, *Adv. Energy Mater.*, 2022, 2103588.
43 O. Snezhkova, F. Bischoff, Y. He, A. Wiengarten, S. Chaudhary, N. Johansson, K. Schulte, J. Knudsen, J. V. Barth and K. Seufert, *J. Chem. Phys.*, 2016, **144**, 094702.
44 S. Kundu, W. Xia, W. Busser, M. Becker, D. A. Schmidt, M. Havenith and M. Muhler, *Phys. Chem. Chem. Phys.*, 2010, **12**, 4351–4359.
45 W. Orellana, C. Zuñiga, A. Gatica, M.-S. Ureta-Zanartu, J. H. Zagal and F. Tasca, *ACS Catal.*, 2022, **12**, 12786–12799.
46 C. Z. Loyola, A. Gatica, N. Troncoso, W. Orellana and F. Tasca, *Electrochim. Acta*, 2024, **473**, 143416.
47 C. Liu, H. Li, F. Liu, J. Chen, Z. Yu, Z. Yuan, C. Wang, H. Zheng, G. Henkelman, L. Wei and Y. Chen, *J. Am. Chem. Soc.*, 2020, **142**, 21861–21871.
48 X. Wang, B. Wang, J. Zhong, F. Zhao, N. Han, W. Huang, M. Zeng, J. Fan and Y. Li, *Nano Res.*, 2016, **9**, 1497–1506.
49 J. Li, M. T. Sougrati, A. Zitolo, J. M. Ablett, I. C. Oğuz, T. Mineva, I. Matanovic, P. Atanassov, Y. Huang, I. Zenyuk, A. Di Cicco, K. Kumar, L. Dubau, F. Maillard, G. Dražić and F. Jaouen, *Nat. Catal.*, 2021, **4**, 10–19.
50 H. Zhang, L. Osmieri, J. H. Park, H. T. Chung, D. A. Cullen, K. C. Neyerlin, D. J. Myers and P. Zelenay, *Nat. Catal.*, 2022, **5**, 455–462.